Galvanostatic Deposition of Iron Powder from Sulfate Electrolytes: Experimental Analysis and Empirical Modeling

Daniela Grigorova[1], Gyunver Hodjaoglu[2], Feyzim Hodzhaoglu[2]

[1]University of Chemical Technology and Metallurgy, 8 Kl. Ohridski Blvd., 1756 Sofia, Bulgaria

e-mail: d.dimitrova@uctm.edu

[2]Institute of Physical Chemistry "Acad. R. Kaischew", Bulgarian Academy of Sciences, Acad. G. Bonchev Str., 1113 Sofia, Bulgaria

ABSTRACT

Producing high-purity iron powders with controlled particle morphology is essential for advanced powder metallurgy, additive manufacturing, and functional materials. However, achieving precise morphological control in environmentally benign, additive-free electrolytes remains challenging. This study systematically investigates the galvanostatic electrodeposition of iron powder from sulfate-based electrolytes containing 10.0 and 50.0 g·L⁻¹ Fe^{2+}, focusing on the interplay between current density, pH evolution, deposition efficiency, and particle structure. A clear transition from compact, adherent deposits at low current densities to dendritic, easily detachable powders at higher values was observed. SEM analysis revealed well-defined dendritic aggregates at 7 $A·dm^{-2}$ (30–80 μm), whereas highly fragmented, porous agglomerates formed at 10 $A·dm^{-2}$, accompanied by fine-scale fragmentation driven by intense hydrogen evolution. XRD confirmed pure α-Fe for current densities up to 7 $A·dm^{-2}$, while partial oxidation to Fe_3O_4 occurred at 10 $A·dm^{-2}$; EDX mapping further supported this surface oxidation. The deposited mass increased linearly with current density for both Fe^{2+} concentrations, with regression models yielding R^2 values above 0.96. Current efficiency decreased at high current densities due to enhanced parasitic reactions. Overall, the results demonstrate that galvanostatic electrodeposition in additive-free sulfate media enables controlled synthesis of iron powders, with tunable morphology and phase purity governed primarily by current density and electrolyte composition.

[DOI: 10.22068/ijmse.4281]

Keywords: iron powder, galvanostatic electrolysis, sulphate electrolyte, SEM morphology; current efficiency.

INTRODUCTION

Iron powders are important raw materials used in powder metallurgy, additive manufacturing, magnetic materials, chemical processing, and pharmaceutical applications [1,2]. Among the available production methods - including atomization, chemical reduction, and electrolysis - the electrolytic route offers high purity together with precise control over particle morphology and size distribution [3,4]. As a result, electrolytic iron powders are particularly suitable for applications requiring controlled microstructure and high reactivity, such as soft magnetic materials, catalysts, and specialty metal blends [5]. Electrolytic deposition of iron in powder form provides significant advantages over conventional compact coatings or films. By controlling electrolysis parameters - especially current density, electrolyte composition, and deposition time - it is possible to promote dendritic, low-adherence deposits that can be readily detached from the cathode and collected as free-flowing powders [6,7]. Although iron electrodeposition has been investigated for decades, systematic studies focused on powder formation in additive-free sulfate electrolytes remain comparatively limited [8,9]. Recent interest has therefore shifted toward environmentally benign electrolyte systems and improved control of powder morphology and electrochemical efficiency [10 - 12].

Galvanostatic deposition, in which a constant current is maintained during electrolysis, represents a practical and reproducible approach for investigating iron powder formation dynamics [13]. The use of sulfate electrolytes without added sulfuric acid or organic additives simplifies the electrolyte composition and reduces the need for complex post-treatment and corrosion control [14,15]. However, such additive-free systems also introduce challenges related to Fe^{2+}/Fe^{3+} conversion, pH drift, hydrogen evolution, and moderate conductivity, all of which influence deposit morphology, phase stability, and current efficiency [10].

This work investigates the electrodeposition of iron powder under galvanostatic conditions using pure sulfate electrolytes at two Fe^{2+} concentrations (10.0 and 50.0 $g \cdot L^{-1}$). Particular attention is given to the relationship between current density, powder morphology, pH evolution, and phase composition. A

[DOI: 10.22068/ijmse.4281]

combined experimental and empirical modeling approach is employed to evaluate iron mass yield and current efficiency under different operating conditions. The deposited powders are characterized by X-ray diffraction (XRD), scanning electron microscopy (SEM), and EDX analysis, while the overall electrolysis process is assessed in terms of stability, efficiency, and morphology control.

MATERIALS AND METHODS

All chemicals used were of analytical grade. Iron (II) sulfate heptahydrate ($FeSO_4 \cdot 7H_2O$) was purchased from Chem-Specter and used without further purification. Two concentrations of aqueous electrolyte were prepared: 10.0 $g \cdot L^{-1}$ and 50.0 $g \cdot L^{-1}$ of Fe^{2+} ions, dissolved in deionized water. No organic additives or free sulfuric acid were added to the solutions in order to maintain an additive-free electrolyte environment. Although potentiostatic control is generally considered suitable for powder deposition due to its ability to maintain a constant overpotential, galvanostatic operation was selected in this study for practical and methodological reasons. This mode enables straightforward process control, reproducible total charge passage, and reflects conditions typical of batch-type industrial systems.

Electrodeposition was performed in a 500 mL borosilicate glass beaker, which served as the electrolysis cell. The cathode was a flat aluminum foil strip (99.9% purity, 0.1 mm thickness) chosen for its low adhesion to iron deposits and ease of powder removal. Two symmetrical lead anodes alloyed with 1% silver (99.9% purity) were used to ensure uniform current distribution. The total cathodic surface area was fixed at 0.35 dm^2. A DC power supply (Amrel LPS 301) provided a constant current. Current values were monitored using a precision ammeter (ML 10), and cell voltage was measured with a Mastech MS8264 multimeter. Stirring and thermal control were provided by a laboratory magnetic stirrer (LLG mini stirrer 3) with an external temperature probe. Electrolysis was performed at room temperature (24-28°C) for 60 min at each selected current density.

The experimental setup (Fig. 1) consisted of a three-electrode electrolysis cell, a DC power supply, a precision ammeter, and a magnetic stirrer with heating control. Electrodes were connected directly to the power source, enabling stable current flow. The mass of deposited iron was determined gravimetrically, and current efficiency was calculated from the applied charge.

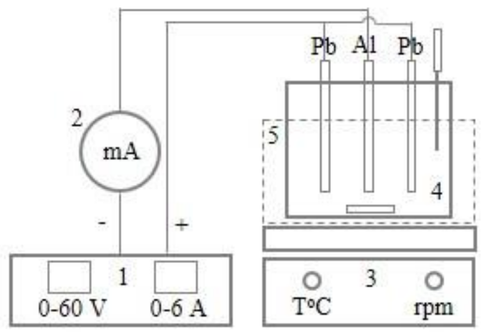

Fig. 1. Schematic diagram of the galvanostatic electrolysis setup used for iron powder deposition. The system includes a DC power supply (1), ammeter (2), magnetic stirrer with heating control (3), a three-electrode cell (4) consisting of two Pb anodes and one Al cathode, and a beaker containing the electrolyte (5)

The applied cathodic current densities (Dk) ranged from 1.0 to 10.0 A·dm^{-2}, corresponding to current values from 0.35 to 3.5 A, respectively. Each deposition was conducted for 60 minutes. Experiments were repeated for both electrolyte concentrations. After electrolysis, deposits were mechanically stripped from the aluminum cathode and collected as free-flowing powder.

Gravimetric measurements were carried out using a Sartorius BP 301 S analytical balance. The electrolyte pH was measured before and after each run using a Crison GLP 22+ pH/Ion meter. Temperature was recorded with the same external probe used for process control. Phase composition was examined by X-ray diffraction (XRD) using a PANalytical Empyrean diffractometer with Cu Kα radiation (λ = 1.5406 Å), scanning in the 2θ range of 20–80°. Microstructural and surface features were analyzed by scanning electron microscopy (SEM) using a Zeiss EVO 10 system operated via SmartSEM Version 7.05 (Service Pack 3).

Theoretical mass yield and current efficiency were calculated using standard electrochemical relations adapted for the galvanostatic regime~~.~~

- Theoretical mass of iron deposited: $G = \frac{ItM}{nF}$, [g] (1)
- Current efficiency: $\eta = \frac{G_{exp,}}{G_{theor}}, 100$ [%] (2)
- Current density was defined as: $D_k = \frac{I}{S}$ (3)

[DOI: 10.22068/ijmse.4281]

Where: I is the applied current (A); t is the electrolysis time (s); M is the molar mass of iron (55.85 g/mol); $n = 2$ is the number of electrons in $Fe^{2+} \rightarrow Fe^{0}$; F is the Faraday constant (96485 C/mol); D_k is the current density $[A \cdot dm^{-2}]$; $S = 0.35\ dm^2$ is the cathode surface area.

RESULTS AND DISCUSSION

Experimental deposition of iron powder was carried out at five current densities (1.0, 3.0, 5.0, 7.0, and 10.0 $A \cdot dm^{-2}$) using sulfate-based electrolytes at two concentrations: 10.0 and 50.0 $g \cdot L^{-1}$ Fe^{2+}. All experiments were conducted for 60 minutes. The resulting iron powder was stripped from the aluminum cathode and weighed. In galvanostatic electrodeposition, the transition from compact metallic deposits to powdery structures typically occurs at high overpotentials, corresponding to the limiting-current region of the polarization curve. The observed behavior is consistent with mechanisms described in the literature for electrolytic iron powder formation [14,15]. The pH of the electrolyte was monitored before and after each deposition cycle. A strong pH drop was observed at higher current densities, attributed to hydrogen evolution and Fe^{2+} oxidation. These effects were more severe in the dilute electrolyte (10.0 $g \cdot L^{-1}$), where pH dropped by up to 1.6 units after 60 min at 10.0 $A \cdot dm^{-2}$. Temperature measurements also revealed moderate increases (up to ~7 °C), with a clear correlation to current density. This thermal effect is caused by ohmic heating and Joule dissipation, further influencing electrolyte stability and morphology of the deposit. The pH and temperature values before and after electrolysis are summarized in Table 1, which shows how both electrolyte systems respond to increasing current density.

Table 1. pH and temperature values before and after electrolysis at different current densities for 10.0 and 50.0 $g \cdot L^{-1}$ Fe^{2+}

I , $A.dm^{-2}$	10.0 $g.L^{-1}$ Fe^{2+}				50.0 $g.L^{-1}$ Fe^{2+}			
	Before electrolysis		After electrolysis		Before electrolysis		After electrolysis	
	pH	T,°C	pH	T,°C	pH	T, °C	pH	T, °C
1.0	3.03	28.3	2.22	28.7	2.78	25.6	2.24	25.7
3.0	3.02	25.5	1.82	31.7	2.94	24.5	1.95	28.0
5.0	3.02	26.7	1.54	30.1	2.85	26.1	1.64	29.4
7.0	3.05	25.2	1.57	28.0	2.75	25.1	1.67	31.0
10.0	3.12	26.1	1.5	33.9	2.75	25.5	1.61	30.7

[DOI: 10.22068/ijmse.4281]

The phase composition of the deposited powders was analyzed by X-ray diffraction (XRD), and the complete diffraction patterns are presented in Fig. 2. For all current densities up to 7.0 A·dm^{-2}, the diffraction patterns confirmed the exclusive presence of metallic α-Fe. At 10.0 A·dm^{-2}, additional peaks corresponding to magnetite (Fe_3O_4) were detected, suggesting partial oxidation of iron either during deposition or in the post-deposition stage. This oxidation is likely associated with elevated local temperatures, pH shifts, or the electrochemical conversion of Fe^{2+} to Fe^{3+} under high-current-density conditions.

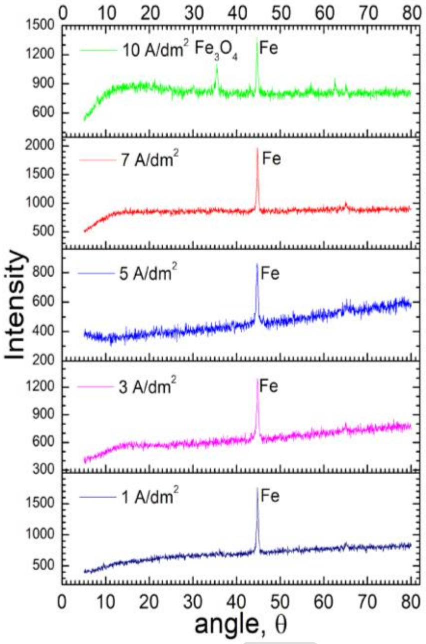

Fig. 2. X-ray diffraction patterns of the iron powders obtained at various current densities, showing formation of Fe_3O_4 at 10.0 A·dm^{-2}.

The morphology of the iron powder obtained at 7 A dm^{-2} is shown in Fig. 3a. The powder consists of compact but clearly dendritic aggregates composed of elongated primary trunks and uniformly distributed secondary branches. The dendrites exhibit well-defined crystalline facets and relatively smooth surfaces, indicating diffusion-limited growth under moderate overpotential. Fragmentation is limited, suggesting that hydrogen evolution does not yet dominate growth disruption. The corresponding EDX Fe map (Fig. 3b) confirms a homogeneous elemental distribution, and the XRD spectrum (Fig. 2) contains only Fe peaks, in agreement with the SEM observations.

[DOI: 10.22068/ijmse.4281]

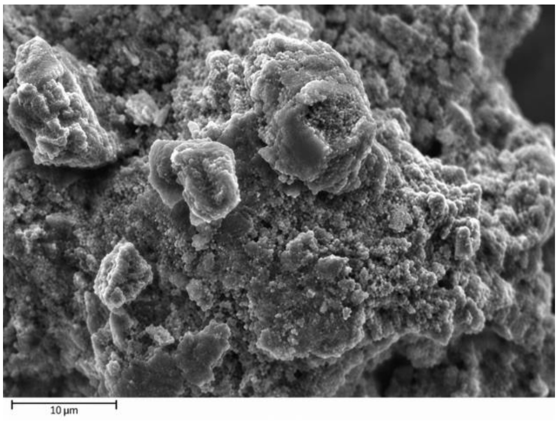

Fig. 3a. SEM morphology at 7 A·dm^{-2}

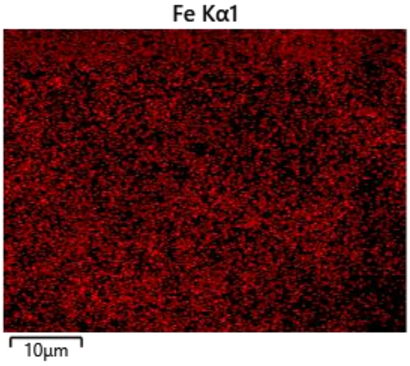

Fig. 3b. EDX Fe map showing uniform Fe distribution at 7 A·dm^{-2}.

At 10 A dm^{-2}, the morphology differs markedly from that at 7 A dm^{-2} (Fig. 4a). Instead of elongated dendrites, the deposit consists of highly fragmented porous agglomerates. This multiscale fragmentation is characteristic of extreme diffusion-limited growth accompanied by intense hydrogen evolution, which disrupts crystallite stability and promotes particle detachment. EDX elemental maps (Fig. 4b) reveal simultaneous Fe and O signals, with oxygen concentrated on the surface, indicating partial oxidation. The EDX spectrum shows a pronounced O–K peak, consistent with the Fe_3O_4 reflections in the XRD pattern (Fig. 2) . The increased fragmentation and porosity therefore reflect both electrochemical and chemical instabilities arising under high overpotential.

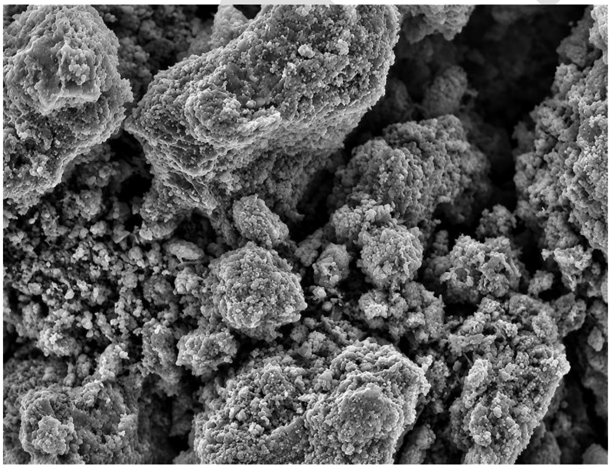

Fig. 4a. SEM morphology at 10 A·dm^{-2}

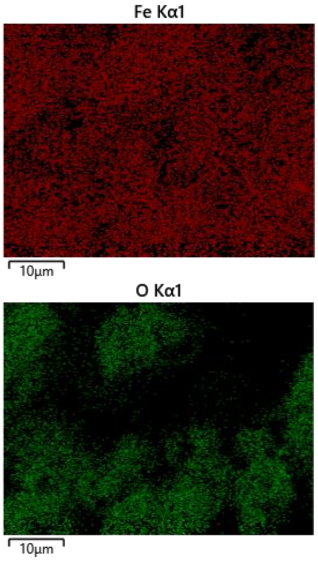

Fig. 4b. EDX. Fe and O maps of the 10 A·dm^{-2} powder

[DOI: 10.22068/ijmse.4281]

The direct comparison of the SEM images (Fig. 5) clearly demonstrates the influence of current density on particle structure. The 7 A dm^{-2} sample retains elongated dendritic structures with limited fragmentation, while the 10 A dm^{-2} powder forms fine, porous clusters with significantly reduced feature size. The morphological shift correlates with the appearance of Fe_3O_4 and the elevated O signal in the EDX maps, confirming that oxidation becomes significant at the highest current density.

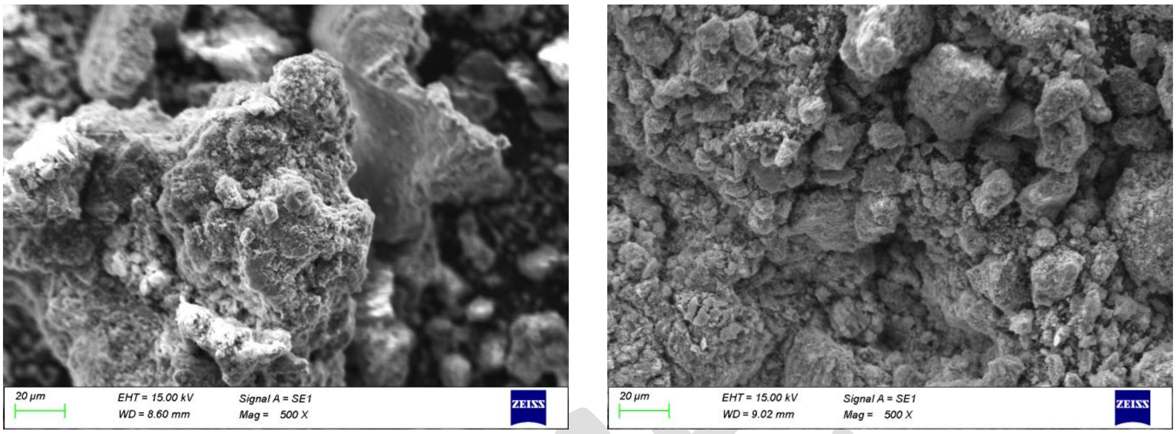

a) 7 A dm^{-2} b) 10 A dm^{-2}

Fig. 5. Comparison of powder morphology at 7 and 10 A·dm^{-2}

At 7 A dm^{-2}, the powder consists of dendritic aggregates 30-80 µm in size. Primary dendritic trunks are 3-7 µm wide, while secondary branches are 1-3 µm. At 10 A dm^{-2}, agglomerates are 10 -35 µm, with fragments of 3-10 µm and finer features of 1–3 µm. These quantitative observations reflect a clear transition from stable dendritic growth to highly fragmented structures driven by increasing current density.

Fig. 6 shows current efficiency as a function of current density. Maximum efficiency (~90%) was observed at 1.0 A·dm^{-2}, while values decline to 35- 60% at 10.0 A·dm^{-2}. The trend highlights the limitations of additive-free sulfate electrolytes and the increasing formation of dendritic and porous structures that reduce electrochemical utilization.

[DOI: 10.22068/ijmse.4281]

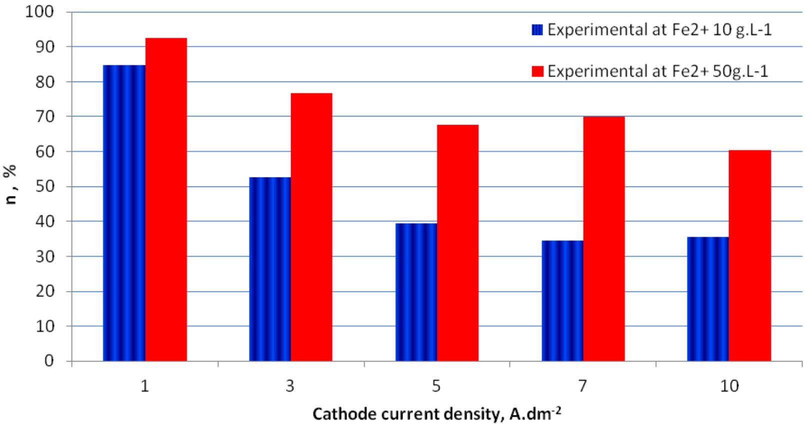

Fig. 6. Current efficiency as a function of applied current density for two Fe^{2+} concentrations.

The relationship between applied current density and the mass of deposited iron powder is presented in Fig. 7. Powder yield increases linearly with current density, especially at higher Fe^{2+} concentrations.

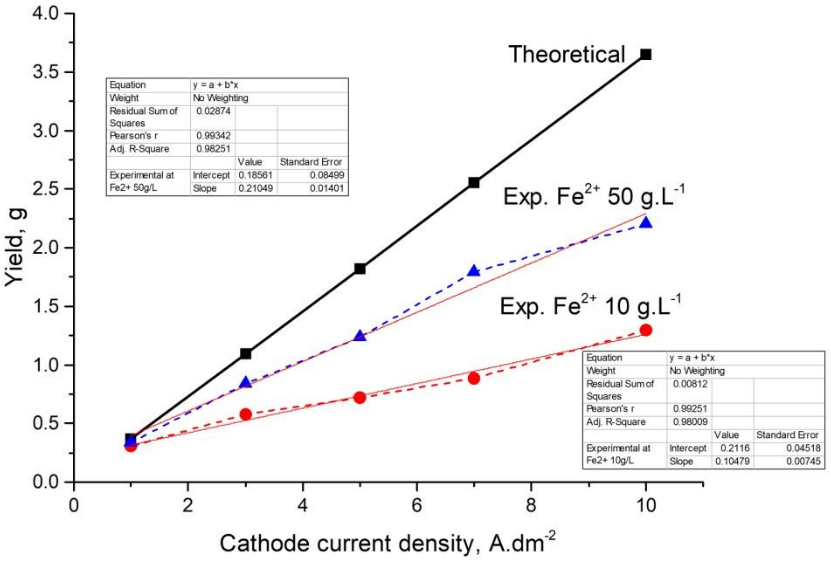

Equation	y = a + b*x		
Weight	No Weighting		
Residual Sum of Squares	0.02874		
Pearson's r	0.99342		
Adj. R-Square	0.98251		
		Value	Standard Error
Experimental at Fe2+ 50g/L	Intercept	0.18561	0.08499
	Slope	0.21049	0.01401

Equation	y = a + b*x		
Weight	No Weighting		
Residual Sum of Squares	0.00812		
Pearson's r	0.99251		
Adj. R-Square	0.98009		
		Value	Standard Error
Experimental at Fe2+ 10g/L	Intercept	0.2116	0.04518
	Slope	0.10479	0.00745

Fig. 7. Comparison between theoretically calculated and experimentally obtained iron powder mass at different current densities for electrolytes containing 10.0 and 50.0 $g\cdot L^{-1}$ Fe^{2+}.

However, this increase is accompanied by decreased current efficiency, indicating stronger side reactions and energy losses at elevated current densities.

[DOI: 10.22068/ijmse.4281]

A clear linear relationship was established between cathodic current density and the mass of deposited iron powder for both investigated electrolyte concentrations. The experimental data were fitted using linear regression [14], resulting in the following empirical equations:

- 10.0 g·L⁻¹ Fe^{2+}: $G = 0.1048 \cdot D_k + 0.2116$
- 50.0 g·L⁻¹ Fe^{2+}: $G = 0.2105 \cdot D_k + 0.1856$

The models correlate well with experimental data (adjusted $R^2 = 0.969$ and 0.982), and comparison with Faraday's law shows increasing deviation at higher currents, consistent with enhanced parasitic reactions. The higher slope of the 50.0 g·L⁻¹ Fe^{2+} regression line reflects improved charge utilization and higher iron yield, likely due to reduced ion transport limitations and better buffering capacity at higher Fe^{2+} concentrations. Conversely, the increasing deviation from the theoretical line at higher current densities can be attributed to parasitic reactions such as hydrogen evolution and partial oxidation of Fe^{2+} to Fe^{3+}, which lower the overall current efficiency.

A three-dimensional response surface (Fig. 8) illustrates the combined effects of pH and current density on yield for both electrolytes. Low Fe^{2+} concentration results in greater yield variability due to stronger sensitivity to pH drift and current fluctuations. In contrast, the 50.0 g L⁻¹ electrolyte provides better buffering capacity, reducing hydrogen evolution and iron oxidation and enabling more stable deposition.

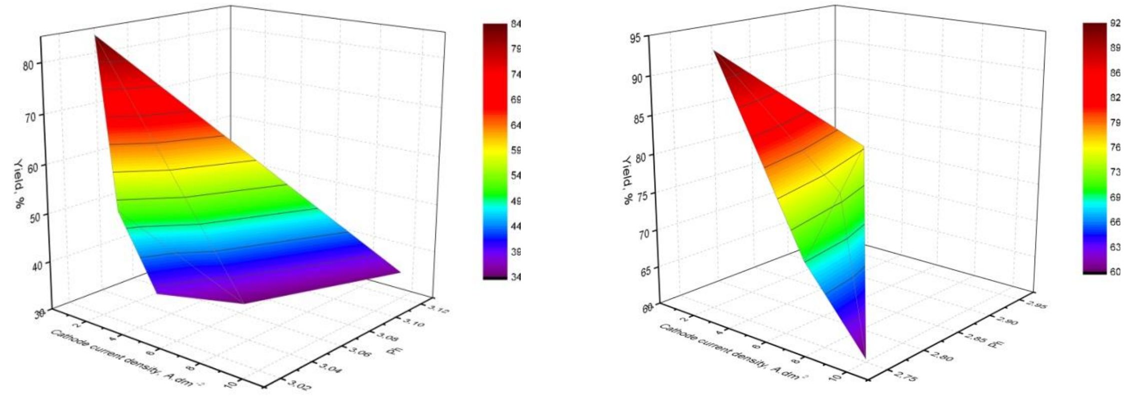

a) 10.0 g.L^{-1} Fe^{2+} b) 50.0 g.L^{-1} Fe^{2+}

Fig.8. (a) 3D response surface of yield (%) vs. cathodic current density and pH for 10.0 g·L⁻¹ Fe^{2+}; (b) Same surface response for 50.0 g·L⁻¹ Fe^{2+}.

[DOI: 10.22068/ijmse.4281]

The electrolyte composition was deliberately chosen to promote the formation of iron powder that could be easily detached from the cathode surface. A relatively low Fe^{2+} concentration was employed, as such conditions favor powdery rather than compact deposits due to diffusion-limited growth. Under these mass-transport-controlled conditions, low ion concentration promotes dendritic structures that readily fragment into powder. It is well established that true powder deposits form only at overpotentials exceeding a critical threshold, where gas evolution and dendritic growth facilitate the detachment of loosely bound particles. Pulse and reverse-pulse electrodeposition techniques have been shown to significantly influence powder characteristics. By modulating the current or potential waveform, grain size and particle morphology can be finely tuned. In particular, periodic polarity reversal induces partial anodic dissolution of protruding dendritic tips, yielding finer, less branched particles with improved dispersibility. Overall, ion diffusion limitations at low Fe^{2+} concentrations play a decisive role in determining deposit morphology, providing a controllable pathway for producing powdery structures.

CONCLUSIONS

In this study, iron powders were successfully produced by galvanostatic electrodeposition from additive-free sulfate electrolytes containing 10.0 and 50.0 $g \cdot L^{-1}$ Fe^{2+}. The simplified electrolyte composition enabled stable deposition conditions, reproducible charge input, and straightforward post-process handling. A strong dependence of deposit morphology on current density was observed. Compact and adherent metallic layers formed at low current densities (1.0–3.0 $A \cdot dm^{-2}$), whereas dendritic, low-adhesion deposits characteristic of powder formation developed above ~5.0 $A \cdot dm^{-2}$. XRD analysis confirmed α-Fe as the dominant phase at current densities up to 7 $A \cdot dm^{-2}$, while partial oxidation to Fe_3O_4 was detected only at 10 $A \cdot dm^{-2}$. SEM observations demonstrated a transition from well-developed dendritic aggregates at 7 $A \cdot dm^{-2}$ to highly fragmented porous agglomerates at 10 $A \cdot dm^{-2}$, reflecting the increasing influence of hydrogen evolution and diffusion limitations at high overpotential. EDX mapping further confirmed homogeneous iron distribution at moderate current density and localized surface oxidation at 10 $A \cdot dm^{-2}$. The mass yield increased linearly with current density for both electrolyte concentrations, with regression models showing strong agreement with the

[DOI: 10.22068/ijmse.4281]

experimental data ($R^2 > 0.96$). At the same time, current efficiency decreased at elevated current densities due to intensified parasitic reactions, including hydrogen evolution and partial Fe^{2+} oxidation. The higher Fe^{2+} concentration (50.0 $g \cdot L^{-1}$) provided improved buffering capacity, lower pH drift, and more stable deposition behavior.

Overall, the results demonstrate that galvanostatic deposition in additive-free sulfate electrolytes provides a simple and reproducible route for controlled synthesis of iron powders with tunable morphology and phase composition. The combined electrochemical, structural, and empirical analyses presented here may serve as a basis for further optimization of iron powder electrodeposition processes and related powder-production technologies.

REFERENCES

[1] German, Randall M. *Powder Metallurgy and Particulate Materials Processing*. Princeton: Metal Powder Industries Federation, 2005.

[2] Chawla, N., and Saini, B., “Recent Advancements in Iron Powder Applications: A Review.” *Mater. Today: Proc.*, 2022, 57, 1154 - 1160. https://doi.org/10.1016/j.matpr.2021.11.327.

[3] Aslanoglu, Z., “Direct Reduction of Mechanically Activated Specular Iron Oxide.”*Miner. Process. Extr. Metall.*, 2013, 114(4), 240 - 244. https://doi.org/10.1179/037195505X81051

[4] Pavlovic, M.; Pavlovic, L.; Nikolic, N., and Popov, K., “The Effect of Some Parameters of Electrolysis on Apparent Density of Electrolytic Copper Powder.” *Mater. Sci. Forum*, 2000, 352, 65 - 72. https://doi.org/10.4028/www.scientific.net/MSF.352.65

[5] Gobber, F.; Bidulská, J.; Fais, A.; Bidulský, R., and Grande, M., “Innovative Densification Process of a Fe-Cr-C Powder Metallurgy Steel.” *Metals*, 2021, 11(4), 665.https://doi.org/10.3390/met11040665.

[6] Maksimovic, M.; Pavlovic, L.; Jovic, B., and Pavlovic, M., “Electrodeposition of Fe Powder from Acid Electrolytes.” *J. Serb. Chem. Soc.*, 2008, 73(8 - 9), 861 - 870. https://doi.org/10.2298/JSC0809861M

[7] Diaz, S., Calderon, L., Barcia, O., and Mattos, O., “Electrodeposition of Iron in Sulfate Solution.” *Electrochim. Acta*, 2008, 53(22), 7426 - 7435. https://doi.org/10.1016/j.electacta.2008.05.033.

[8] Djokić, S. S. (Ed.). Electrochemical Production of Metal Powders. Modern Aspects of Electrochemistry. Springer, New York, 2012. https://doi.org/10.1007/978-1-4614-2380-5

[9] Luchcińska, S.; Lach, J.; Wróbel, K.; Łukomska, A.; Łoś, P., "The recovery of metals as high value powders and nanopowders from industrial wastewaters using potential-controlled electrolysis." *Int. J. Environ. Sci. Technol.*, 2023, 20(7), 7117 - 7132. https://doi.org/10.1007/s13762-022-04401-7

[10] Nikolić, N. D.; Maksimović, V. M.; Avramović, L., "Correlation of Morphology and Crystal Structure of Metal Powders Produced by Electrolysis Processes." *Metals,* 2021, 11(6), 859. https://doi.org/10.3390/met11060859

[11] An, J.; Xie, G.; Xia, W.; Wang, H.; Ren, B.; Liu, K., "Preparation of fine copper powders by galvanostatic regime of electrolysis of copper scrap in a cylindrical electrochemical cell." *Powder Technol.*, 2021, 386, 193 - 198. https://doi.org/10.1016/j.powtec.2021.03.034

[12] Torabinejad, V.; Aliofkhazraei, M.; Allahyarzadeh, M.; Sabour Rouhaghdam, A., "Electrodeposition of Ni - Fe alloys, composites, and nano coatings -A review," *J. Alloys Compd.* 2017, *691*, 841 - 859. https://doi.org/10.1016/j.jallcom.2016.08.329

[13] Murphy, S. V.; Hibbert, D. B., "A model of the anodic behaviour of iron in aqueous media." *Phys. Chem. Chem. Phys.*, 1999, 1(22), 5163 - 5167. https://doi.org/10.1039/A904192C

[14] Kityk, A.; Pavlik, V.; Hnatko, M., "Breaking barriers in electrodeposition: Novel eco-friendly approach based on utilization of deep eutectic solvents." *Adv. Colloid Interface Sci.*, 2024, 334, 103310. https://doi.org/10.1016/j.cis.2024.103310

[15] Siwal, S. S.; Kaur, H.; Deng, R.; Zhang, Q., "A review on electrochemical techniques for metal recovery from waste resources." *Curr. Opin. Green Sustain. Chem.*, 2023, 39, 100722. https://doi.org/10.1016/j.cogsc.2022.100722

[16] Kleinbaum, D. G.; Kupper, L. L.; Nizam, A.; Rosenberg, E., *Applied Regression Analysis and Other Multivariable Methods*, 5th ed., Cengage Learning, Boston, MA, USA, 2014. ISBN: 978-1-305-27015-0.

[DOI: 10.22068/ijmse.4281]